A transmission X-ray microscopy and NEXAFS approach for studying corroded silicate glasses at the nanometer scale

Authors:

M.Kutzschbach[1,2,*], P.Guttmann[3], K. Marquardt[4], S. Werner[3], K. D. Henzler[5], M. Wilke[2,6]

[1]Fachgebiet Mineralogie-Petrologie, Technische Universität Berlin, 13355 Berlin, Germany

[2]Deutsches GeoForschungsZentrum Potsdam, 14473 Potsdam, Germany

[3]Helmholtz-Zentrum Berlin für Materialien und Energie, Institute for Soft Matter and Functional Materials, 12489 Berlin, Germany

[4]BGI, Bayrisches Geoinstitut, Universität Bayreuth, 95447 Bayreuth, Germany

[5]Paul Scherrer Institut, Laboratory for femtosecond chemistry, 5232 Villigen PSI, Switzerland

[6]Institut für Erd- und Umweltwissenschaften, Universität Potsdam, 14476 Potsdam, Germany

*E-mail: mkutz@gfz-potsdam.de

ABSTRACT

In this study transmission X-ray microscopy (TXM) was tested as a method to investigate the chemistry and structure of corroded silicate glasses at the nanometer scale. Three different silicate glasses were altered in static corrosion experiments for 1-336 hours at temperatures between 60°C and 85°C using a 25% HCl solution. Thin lamellas were cut perpendicular to the surface of corroded glass monoliths and were analysed with conventional TEM as well as with TXM. By recording optical density profiles at photon energies around the Na and O K-edges, the shape of the corrosion rim/pristine glass interfaces and the thickness of the corrosion rims has been determined. Na and O near-edge X-ray absorption fine-structure spectra (NEXAFS) were obtained without inducing irradiation damage and have been used to detect chemical changes in the corrosion rims. Spatially resolved NEXAFS spectra at the O K-edge provided insight to structural changes in the corrosion layer on the atomic scale. By comparison to O K-edge spectra of silicate minerals and (hydrous) albite glass as well as to O K-edge NEXAFS of model structures simulated with *ab initio* calculations, evidence is provided that changes of the fine structure at the O K-edge are assigned to the formation of siloxane groups in the corrosion rim.

1. INTRODUCTION

Just as any mineral, glasses are subject to physical degradation and chemical conversion. Glasses are ubiquitous in nature as a product of volcanic activity. For instance, basaltic magmas produced at Mid Oceanic Ridges are quenched to glass in contact with seawater and form hyaloclastic deposits (Fischer and Schmincke 1984). Their dissolution largely contributes to the elemental budget of ocean water. Continental volcanic activity results in large-scale deposition of ashes or pumice with a large fraction of vitreous components. For instance, silica-rich magmas have produced large deposits of obsidian as in the northern part of Lipari island, Italy. Soils developed on these volcanic bedrocks are known to be very fertile as nutrients like phosphorous are easily leached (Dahlgren et al. 2004).

In Industry, corrosion of glass remains a challenge for producing chemically durable glassware. The yield strength of glasses decreases dramatically by surface scratches and strength recovery by crack healing is inhibited if crack surfaces are altered (Wiederhorn and Townsend, 1970). Moreover, glass corrosion leads to a loss of transparency, which is one of the key factors governing the efficiency of photovoltaic modules and is considered a nuisance particularly on valuable glassy tableware. Finally and most severely, corrosion of borosilicate glasses used for the storage of radioactive waste may cause radioactive elements to be released into groundwater (Werme et al. 1990).

The only way to assess the dynamics of glass corrosion on time-scales of hundreds and thousands of years is by computational modeling. Hence, fundamental understanding of the corrosion mechanism on the atomic scale is of crucial importance to build reliable models. So far, the most commonly accepted conceptual model has been introduced by Grambow (1985). It is based on interdiffusion of network modifying cations (those cations that do not enter the

3

tetrahedral site of the polymeric network in silicate glasses) and water, which creates a leached surface layer. As of final result of this interdiffusion process, a so-called "Gel layer" forms by subsequent polymerization reaction of Si-OH (Silanol) to Siloxane (Si-O-Si). Contrary, Geisler et al. (2010) and Hellmann et al. (2012, 2015) describe glass corrosion as a dissolution/re-precipitation process. They claim that dissolution of the pristine glass happens within a thin, i.e. a few molecular monolayers, fluid film of water in contact with the glass. As soon as saturation is reached the "Gel" phase directly precipitates from the solution. The "Gel" is mainly composed of amorphous silica and network-modifying cations (Na, Mg, Ca) remain in the solution within the pores and are transported by diffusion through the fluid in the connected pore space into the bulk solution. The reaction front moves further into the pristine glass, which causes an ongoing growth of the porous "Gel" Layer.

Independent of the conceptual model, studies on silicate glass dissolution kinetics often show a sudden drop in dissolution rates by several orders of magnitude as soon as dissolved silica is sufficiently concentrated in the solution (about 1 mg/L at 90°; Frugier et al. 2008). Some authors attribute the drop to the passivizing effect of an evolving dense alteration layer or corrosion rim on the glass surface (e.g. Rebiscoul et al., 2004; Jégou et al., 2000; Cailleteau et al., 2008), whereas other groups argue that the drop is related to the approach of chemical equilibrium between glass and solution as more and more glass constituents are transported to the solution (e.g. Grambow & Müller, 2001; Bourcier et al., 1990; Munier et al., 2004). Recent findings of Cailleteau et al. (2008) suggest that the drop in the corrosion rate might correspond to structural changes, i.e. densification within the corrosion rim. They also report that this drop in the dissolution rate may be completely absent, depending on the glass composition.

The latter results show that careful studies of the chemistry, structure and structural changes within the corrosion rim are of great importance as it largely governs the dissolution

behavior of silicate glasses. At the same time, related studies have been very rare, still (e.g. Rebiscoul et al. 2004, Gin et al. 2013, Valle et al. 2010, Parruzot et al. 2015, Hellman et al. 2015; Le Guillou et al. 2015). Interestingly, most of the latter studies apply sophisticated analytical tools (e.g. time of flight secondary ion mass spectroscopy, tomographic atom probe, X-ray reflectometry or Rutherford back-scattering). This is, amongst others, owed to the limitations during *in situ* analysis of altered silicate glasses at high spatial resolution by conventional transmission electron microscopy. The high-energy electron beam of a transmission electron microscope (typically 200 kV), often leads to vaporization of the delicate glasses and/or internal crystallization or phase separation (DeNatale & Howitt 1984; Manara et al. 1984; Jiang et al. 2003). A possibility to overcome problems of irradiation damage would be the use of a TEM providing acceleration voltages <200 kV (e.g. Super STEM in Daresbury; SALVE III microscope at the Ulm University; Stöger-Pollach, 2010; Majorovits et al. 2016), which, however, has not been recognized for the study of silicate glasses, yet, to our best knowledge. Another possibility, is to use energy filtered TEM (EFTEM) or TEM electron energy loss spectroscopy (EELS), which both have been successfully applied to derive chemical information of altered silicate glasses at the nanometer scale (Hellman et al. 2015, Gin et al. 2013). A severe disadvantage of TEM EELS is the modification of the molecular glass structure upon irradiation, which is evident from changes in the spectral shape of for example boron K-, or oxygen K-edges with increasing irradiation time (e.g. Jiang et al. 2003, Sun et al. 2004, Cheng et al. 2015). This is unfortunate, because EELS is a versatile tool for characterizing the coordination chemistry, particularly in non-crystalline compounds.

Here, we discuss the characterization of altered silicate glasses by high-resolution transmission X-Ray microscopy (TXM) and combined X-Ray absorption near-edge spectroscopy (NEXAFS), which provides structural information of pristine glasses and corrosion rims on the

molecular scale similar to TEM EELS. By applying soft X-Rays as a probe, we show that chemical characterization using shape and height of X-ray absorption edges is possible, without altering the delicate corrosion layers during the analytical procedure. At the same time, information can be collected with a spatial resolution down to 10 nm.

2. GLASS SYNTHESIS AND CORROSION EXPERIMENTS

2.1 Glass synthesis. 100 g of two different silicate glasses were synthesized from a mixture of SiO_2, $Al_2(OH)_3$, Na_2CO_3, $CaCO_3$ and $MgCO_3$. By normalization to 8 oxygens their compositions are: $Na_{0.14}Ca_{0.74}Mg_{0.38}Al_{2.10}Si_{1.83}O_8$, termed "Ab15" in the following, and $Na_{0.84}Ca_{0.10}Mg_{0.09}Al_{1.04}Si_{2.92}O_8$, termed "Ab90". Prior to weighing, powders were dried over night at 110°C. Homogenization was achieved in 15 minutes by crushing in an agate mortar under aceton. Glasses were fused in corundum crucibles, at ambient pressures and 1750°C for 3 hours. Glasses where ground again to grain size < 0·5 mm and filled into platinum tubes of 5 cm length and 1 cm diameter, which were welded from one side. Glasses were molten in Pt Tubes for another 24 hours at 1500°C (Ab90) and 1600°C (Ab15). Peak temperatures have been reached after 2 hours. Platinum tubes were immediately transferred into a cooling oven at temperatures 50°C above glass transition temperatures calculated with the SciGlass database (665°C for Ab90, 756°C for Ab15). After 2 hours of relaxation time, the oven was shut down and glasses cooled slowly to ambient temperature. Platinum was removed and glass molds were cut into 1·5 mm thick disks, which were polished from both sides.

2.2 Corrosion experiments. 5 glass disks were hooked with Teflon wire on a teflon holder. A teflon reactor was filled with 2 liters of 25% HCl and placed into a heating stage filled

up with quartz sand for isolation and homogeneous temperature distribution. The heating stage was equipped with a magnetic stirrer and heated to 85°C. Temperature was measured every 2-8 hours with a glass thermometer. After the peak temperature was reached, the holder with the glass disks was inserted and the reactor was closed. Prior to the experiments, every experimental part was carefully cleaned with isopropanol and finally rinsed several times with distilled water. Duration of the experiments was 1 hour for Ab15 and 336 hours for the Ab90 glass. After removal, the glass disks were carefully rinsed with iso-propanol and distilled water

The technical glass, termed "TG" in the following, was originally only used to test the experimental and TXM analytical protocol, and thus was treated differently to the other samples. We still report the results because they highlight that the development of corrosion layers may - vary considerably, depending on composition and/or conditions. The technical glass consists of a piece of an object slide usually used for rock thin section preparation. A piece of about 2 x 1 cm^2 with a thickness of about 2 mm was used. As the surface was already smooth, the glass piece was altered without any further polishing in a borosilicate glass flask filled with 400 ml 25% HCl solution at 60°C. The solution was not stirred during the experiment. After 192 hours the glass piece was removed and rinsed with iso-propanol and distilled water.

3. ANALYTICAL TECHNIQUES

3.1 Transmission electron microscopy (TEM). Electron transparent lamella were prepared with the focused ion beam (FIB) technique. Details of the FIB sample preparation are given elsewhere (Wirth, 2004).

Transmission electron microscopy (TEM) was performed in a Tecnai F20 X-twin with a Schottky field emitter as electron source. The TEM was operated at 200 kV. High-angle annular dark field

(HAADF) imaging was performed in Z-contrast imaging mode using a camera length was optimized to obtain maximum Z-contrast. The HAADF detector is a Fishione system. EDX analyses were acquired with an EDAX detector with ultrathin window. All EDX profiles were acquired in the scanning transmission mode (STEM) scanning the electron beam in a small (400 × 10 nm) window to reduce mass loss during the measurement. To maximize the EDX signal, the sample is tilted with a 15° angle towards the EDX detector. The rotation axis was chosen to be about perpendicular to the pristine glass/corrosion rim interface, to prevent the electron beam from passing through corrosion rim and pristine glass simultaneously. Pixel size during measurements was varied between 0·5 nm to 4 nm. The optimized probe size in STEM at this microscope is 3·8nm using a C2 of 50μm and a gun lens number of 7.

3.2 Transmission X-Ray Microscopy (TXM) and X-Ray absorption near edge Spectroscopy. X-ray absorption images and NEXAFS Spectra were acquired at the BESSY II electron storage ring of the Helmholtz Zentrum Berlin (Beamline: U41-TXM). The storage ring was operated in top-up mode with the beam current varying between 250 and 300mA over the course of our beamtime. The beamline is equipped with a full-field transmission x-ray microscope that allows imaging of samples, which are transparent for photons in the soft X-ray energy range (250-1500 eV). Preparation procedure for the samples is basically the same as for the TEM investigations. Here, each lamella was cut by FIB into a step-like shape with three different thicknesses (0·2, 0·5 and 1 μm) to maintain photon transparency and an optimum signal/noise ratio at all photon energies. Lamellas were placed on a holey carbon grid. As the TXM uses a modified CompuStage from FEI Company, regular TEM holders can be used for inserting the sample (Guttmann et al. 2012).

The monochromatic X-radiation was focused onto the sample with a capillary condenser. To illuminate the whole sample area the beam is moved across the specimen in a spiral shape. Transmitted X-Rays are projected via an objective zone plate lens onto a CCD camera, which produces the final image. The field of view is 13-20 μm^2 and the image pixel size corresponds to a real size between 6·3 nm and 14·5 nm. The sample position is fixed, whereas the objective zone plate and the CCD Camera are moveable. Their free scope limits the maximum magnification at a given photon energy (e.g. 1380x at 1090 eV and 2020x at 530eV).

Photon energies can be varied with an energy resolution of about $E/\Delta E = 10^4$ depending on the vertical opening of the exit slit width after the monochromator. Having a sufficient photon flux, but preserving the desired spectral resolution we worked with an energy resolution of $E/\Delta E = 0·6 \times 10^4$ at the O K- Edge and $E/\Delta E = 0·24 \times 10^4$ at the Na K- Edge. The exposure time for a single image varies between 2 seconds (O K- edge) and 8 seconds (Na K- edge).

To obtain O K-edge NEXAFS spectra, several images were recorded in steps between 520-550 eV with $\Delta E=0·2$ eV and between 550-580 eV with $\Delta E=0·5$ eV. Na K-edge NEXAFS were obtained by recording images between 1060-1080 eV with $\Delta E=1·0$ eV, between 1070-1085 eV with $\Delta E=0·75$ eV and between 1085-1100 eV with $\Delta E=1·0$ eV. The images were combined to stacks, which were aligned using the aXis2000 software package (Hitchcock et al. 1997). We used a pixel-binning factor of 2, which resulted in an increase of image pixel size (12·5 -29 nm), but improved the signal/noise ratio. Within the image stack, the region of interest was set and averaged grey values of this region yielded the transmitted X-Ray intensity (I_{trans}). Similarly the background intensity I_0 was obtained from some region outside of the sample. The optical density (OD) is calculated with:

$$(1) \qquad OD = -\ln\left(\frac{I_{trans}}{I_0}\right) = \mu \times d$$

with *d* being the thickness of the glass lamella and μ the absorption coefficient. Within a glass lamella, spectra of corrosion rim and pristine glasses were always collected from regions with equal thicknesses. For processing the spectra, a straight pre-edge background was subtracted and the edge jump was fitted with an *arctan* function.

3.3 *Ab initio* modeling with FDMNES computer code. The calculated O K- edge spectra presented in this study where simulated using the FDMNES computer code (Burnau & Joly, 2009). With the help of this *ab initio* approach the electronic structure of the absorbing atom can be calculated on the basis of the density functional theory. The program was run in finite difference mode, *i.e.* with a free shape of the atomic potentials. The final electron states are calculated considering only interactions with atoms inside a sphere with a radius of 3·5 Å. The Fermi Energy was set to -5·5 eV. The resulting spectrum is a weighted summation of contributions from all the O atoms in the structure. Spectra are convoluted with an arctangent function, accounting for the core level width and the energy dependent broadening of the final state width. Subsequently, E_0 was calibrated to the E_0 of the reference Quartz spectrum ($E_0 = 537$ eV), just as done for the calibration of the experimental O K-edge NEXAFS spectra.

4. RESULTS

4.1 Composition of pristine glasses. Pristine glass compositions were determined from 50-80 individual electron microprobe measurements. Investigations under polarized light revealed that crystalline compounds are absent, which is confirmed by the absence of diffraction peaks in the powder diffraction patterns as well as by TEM. Glass compositions are compiled in Table 1.

4.2 Thickness of corrosion rims and transition to the pristine glasses.

Evaluation of TEM images was performed on the basis of HAADF contrast images (Fig. 1a, b), which depends on the thickness of the lamella as well as the mean atomic number and porosity of the material under investigation. For TXM, optical density maps were used (Fig. 1c-f), which were prepared as described in the methods section. Because the Ab90 glass has not developed a corrosion rim after 336 hours of alteration, we focus on the results for the Ab15 glass altered for 1 hour and the TG sample altered for 192 hours. To determine the corrosion thickness and the shape of the interface between corrosion rim and pristine glasses, 20 grey scale profiles were recorded perpendicular to the corrosion rim/pristine glass interface using the imageJ software package. After alignment, the profiles were interpolated and averaged (Fig. 2) and both, the transitions from corrosion rim to the pristine glass (rim→pri) and from corrosion rim to the carbon layer (rim→C) were fitted with a sigmoidal function (Fig. 3). The contrast c (optical density or HAADF) at position x between maximum (c_{max}) and minimum (c_{min}) contrast is modeled with:

(2)
$$c(x) = \frac{c_{max}}{\left[1 + \exp\left(\frac{x_{infl} - x}{S}\right)\right]} + c_{min}$$

with x_{infl} being the position of the inflection point and S the steepness of the curve. Finally, we normalized each sigmoidal function to go from $c_{min}=0$ to $c_{max}=1$. The rim thickness is then defined as the distance between the two inflection points (Fig. 3). In case the carbon layer is not resolved in the contrast profile (at 1080 eV), we fitted the transition from the corrosion rim to the platinum layer (rim→Pt) to locate the second inflection point. The sum of the errors on the position of each inflection point is better than 2 nm within a 95% confidence interval. In addition to the rim thickness, we also determined the transition width, i.e. the distance from one contrast plateau to another (Table 2). Transition widths were determined on the basis of the normalized

11

fitted sigmoidal functions taking the distance between 5% and 95% of the maximum contrast c_{max} (Fig. 3). Relevant transitions are from the corrosion rim to the carbon layer (rim→C), from the corrosion rim to the pristine glass (rim→pri), and from either the carbon layer or the corrosion rim to the platinum layer [(rim)/C→Pt] depending on whether or not the carbon layer is resolved.

4.2.1 Effective spatial resolution

Both, results for rim thickness and transition width are likely biased by the spatial resolution of the imaging technique, which is a convolution of the pixel size of the CCD detector and the resolution of the zone plate (TXM) or the electron beam size (TEM), respectively. If for example the spatial resolution exceeds the thickness of a layer, this layer may not be resolved in the corresponding contrast profile.

The spatial resolution is even more critical for the determination of the transition width. This is shown in Figure 4a, where we modeled contrast profiles for the theoretical case, in which a perfectly step-like transition is imaged with a beam having a Gaussian shaped intensity profile and different full width at half maximum (FWHM). As illustrated in Figure 4b, transition width and spatial resolution, *i.e.* FWHM of the Gaussian-shaped beam, are linearly correlated by the following equation:

(3) $$\text{transition width} = 1 \cdot 43 \times \text{spatial resolution}$$

Another cause for a broadening of transition profiles are off-perpendicular orientations between layer boundaries and the incoming beam. Although problems due to misorientation are minor during TEM investigations, they might worsen spatial resolution during TXM imaging.

In order to quantify the effective spatial resolution for the different imaging methods, we used the width measured at the C→Pt and (rim)/C→Pt transitions, which are both considered sharp within a few nm. The effective spatial resolution is then defined as the FWHM of a Gaussian shaped

beam needed to produce a theoretical contrast profile with equal transition width. Applying equation (3), yields effective spatial resolution that varies between 24 nm for TEM HAADF imaging and 78 nm for TXM imaging at 1080 eV (Fig. 5, Table 2). In case of TXM imaging at 536 eV and TEM, multiple results for the effective spatial resolution are obtained, based on the sharp rim→C and C→Pt transitions in Ab15 and TG glasses (Table 2). By calculating the standard deviation (1 SD), we estimate the accuracy of the effective spatial resolution to be better than 40%.

4.2.2 Rim thickness and transition width determined with TEM. Examinations of the altered glasses with TEM reveal that only the Ab15 and TG glasses have developed a corrosion rim. Its thickness is 316 nm for the Ab15 glass after 1 hour of alteration and 126 nm for the TG sample after 192 hours of alteration (Fig. 1a, b; Fig. 2; Table 2). Towards the contact to the protective Platinum layer (high intensity) deposited prior to FIB milling for surface protection, the corrosion rim is followed by a ~20 nm wide stripe with low intensity value, which stems from the Carbon that has been deposited prior to the SEM imaging. Whereas the Ab15 corrosion rim exhibits extensive porosity with individual pores reaching up to 10 nm in size (Fig. 1a), the corrosion rim of the TG sample appears non-porous (Fig. 1b). The contact between pristine glasses and corrosion rims in the Ab15 glass is sharp and the contrast transitions within a width of 58 nm (Fig. 6, Table 2). Contrary, the transition between corrosion rim and pristine glass in the TG sample extends over almost twice the length (106 nm).

4.2.3 Rim thickness and transition width determined with TXM. In Figure 1 (c-f) we present optical density images at photon energies of 536 eV (O K-edge) and 1080 eV (Na K-edge) with lighter areas corresponding to regions with high optical density and darker areas corresponding to regions with low optical density. At both photon energies, a corrosion rim is visible. However, only at 536 eV the thin Carbon film can be recognized (Fig. 1c,d; Fig. 2). At

13

536 eV, the corrosion rim of the Ab15 glass is about 30 nm thicker (345 nm) than the thickness obtained from TEM (Fig. 6a). At photon energies of 1080 eV, the corrosion rim appears even wider with a thickness of 397 nm. Compared to the TEM results, the transition from corrosion rim to the pristine glass extends over a larger range of 78 nm at 536 eV and 104 nm at 1080 eV (Fig. 6b; Table 2). Whereas, the pores in the Ab15 corrosion rim remain unresolved (Fig. 1c, e), the corrosion rim of the TG sample can be visualized with TXM at both photon energies. The thickness of its corrosion rim determined at 536 eV (136 nm) is closely matching the TEM value (Fig. 6a, Table 2). However, at a photon energy of 1080 eV, a higher thickness of about 175 nm is found. Similar to the TEM results, the boundary between corrosion rim and pristine TG sample appears not as sharp as in the Ab15 glass. This is confirmed by the optical density profiles at 536 eV and 1080 eV (Fig. 2), revealing a more gradual drop in X-ray transmission compared to the Ab15 glass (116 nm at 536 eV and 140 nm at 1080 eV; Fig. 6b, Table 2).

4.3 Determining compositions of corrosion rim with TEM. Determining accurate chemical compositions of the corrosion rim using TEM-EDX was impossible, since the delicate corrosion rims vaporized during EDX spectra acquisition (Fig. 7), although we applied STEM scanning over a window. Even increasing the window size to 400×60nm could not prevent severe mass loss during acquisition of the spectra (Fig. 7b). Another problem is the crystallization of glass induced by the electron beam (Fig. 7c), which likely causes compositional inhomogeneity. Therefore, our TEM-EDX data can only be evaluated on a qualitative basis and, due to the mass loss, only if K_α intensities of the element of interest are normalized to some reference K_α-intensity. For this reason, all TEM-EDX data presented in this study were normalized to the Si K_α-intensity. As a measure for the intensity, we used the area of the Gaussian peaks fitted to the EDX spectra. Due to the very thin corrosion rim layer in the TG sample we measured three

14

individual EDX profiles, which were taken from different regions and for the Ab15 glass we acquired only one profile (Fig. 8).

The Ab15 glass displays a strong increase in relative O concentrations. For all other elements, a rather sharp concentration decrease has been noticed compared to the pristine glass (Fig. 8a). Local maxima in Ca K_α-intensity observed in the upper section of the Ab15 corrosion rim are probably due to $CaCl_2$ that precipitated in the pore space. In the TG sample, Na is highly depleted in the corrosion rim with a rather smooth increase towards the pristine glass. Similar to the Ab15 glass, the TG sample shows enrichment in O in the corrosion rim, although it is not as pronounced as in the corrosion rim of the Ab15 glass. All other elements not presented here were below the detection limit.

4.4 Determining compositions of corrosion rim with TXM. As the interaction between glasses and soft X-rays is much less destructive, we tried to derive compositional information from X-Ray transmission images recorded with the TXM. This was done on the basis of the edge jumps ($\Delta\mu d$) across Na and O K-edges (Fig. 9). The height of the edge jump is proportional to the number of atoms of an element e per unit area (C_A), which can be calculated by normalizing the volume concentration (C_V) of an element e to the thickness (d) of the glass foil (equation 3). The volume concentration (C_V) of the element e is a function of effective density (ρ_{eff}), such as molar concentration of e (X_{mol}) in pristine glass and corrosion rim, respectively (equation 4)

$$(4) \qquad \Delta\mu d \sim C_A(e) = C_V(e) / d$$

$$(5) \qquad C_V(e) = [\rho_{eff} \times X_{mol}(e) \times N_A] / M(e)$$

with *M(e)* being the standard atomic weight of element e and N_A the Avogadro constant. Assuming that all void space is filled with air, the effective density is defined as:

$$(6) \qquad \rho_{eff} = \rho_{particle}(1-\Phi)$$

All lamellas used for investigation at a given absorption edge were cut with the same thickness.

Hence, changes in Δμd between pristine glasses and corrosion rims within the same and between different glass samples do not depend on thickness and are solely due to changes in particle density ($\rho_{particle}$), porosity (Φ) or molar concentrations of the element of interest. Edge jumps were derived from fitting of an *arctan* function to the Na and O K-edge NEXAFS spectra, which were obtained by the procedure described in the methods section. Results are compiled in Table 3 and Figure 10.

4.4.1 Edge jump at O K-edge. The transition between corrosion rim and pristine glass of the Ab15 glass is marked by an increase in the Δμd of 40% from 0·48(1) in the corrosion rim to 0·67(1) in the pristine glass at a lamella thickness of 200 nm (Fig. 10). In the TG sample the transition from pristine glass to corrosion rim is subtler and recognized by a decrease in the average Δμd of 17% from 0·76(1) in the corrosion rim to 0·63(1) in the pristine glass (Fig. 10) at a lamella thickness of 200nm.

4.4.2 Edge jump at Na K-edge. Here, edge jumps are always lower in the corrosion rims than in their pristine counterparts. The decrease is more pronounced in the TG sample with Δμd decreasing from 0·21(3) to 0·12(2). In the Ab15 glass Δμd decreases from 0·04(2) in the corrosion rim to 0·02(1) in the pristine glass, which is an insignificant change within errors.

To ultimately derive compositions from TXM images, we plotted the edge jumps (Δμd) of the pristine glasses against compositions derived by electron microprobe analysis (Fig. 11). The latter were recalculated as atoms/cm^2 using equation (4) and (5) with glass densities from Fluegel (2008) for Ab15, Ab90, TG and dry Ab100 glasses and Orlova (1964) for Ab100 glass with 5 wt% H_2O (Table 3). Based on this calibration we were able to obtain concentration per unit area (C_A) of O and Na inside the corrosion rims (Table 3). For the corrosion rim of the Ab15 glass, we detected a decrease in the area concentration of O from $1·23 \times 10^{18}$ to $0·91(9) \times 10^{18}$ atoms/cm^2, which is opposite to the increase in relative O K_a intensities determined with TEM. Area

concentrations of Na decrease insignificantly from 0.08×10^{18} to $0.06(1) \times 10^{18}$ atoms/cm^2. In the TG sample, area concentration of O increases from 1.11×10^{18} atoms/cm^2 in the pristine glass to $1.47(15) \times 10^{18}$ in the corrosion rim. In contrast, a strong decrease of the Na concentration from 0.66×10^{18} to $0.38(6) \times 10^{18}$ atoms/cm^2 in the TG sample corrosion rim has been detected.

4.5 NEXAFS Spectra (O K- edge). Oxygen K-edge spectra were recorded for the Ab15 glass and the TG sample in corrosion rim and pristine areas, respectively. As reference, the O K- edge NEXAFS spectra of natural quartz and natural olivine were measured (Fig. 12). Threshold energies of all other O K- edge NEXAFS spectra given in this study were calibrated using the threshold energy (E_o) of quartz, which was determined taking the inflection point of the edge jump at $E_0 = 537$ eV. NEXAFS peak positions are given relative to the threshold energy as ΔE_0. For comparison, also two reference spectra of a dry Albite glass ($NaAlSi_3O_8$) and an Albite glass containing 5 wt% H_2O were acquired (Fig. 13).

The main-edge maximum comprises two features (*a* and *b*). Feature *a* is located between $1.4 - 2.2$ eV, whereas the position of feature *b* is between $4.8 - 5.2$ eV. The splitting between peak *a* and *b* is highest in pristine Ab15 glass ($\Delta E = 3.4$ eV) and decreases in its corrosion rim ($\Delta E = 2.6$ eV). The TG sample shows a similar but less apparent narrowing ($\Delta E = 3.0$ eV in the pristine glass, 2.6 eV in the corrosion rim). In all of the spectra, feature *a* is more intense (by height) than feature *b*, except in the Ab15 corrosion rim and in the dry Albite glass where feature *b* is more intense.

The location of a third feature *c* does not exhibit any resolvable differences between pristine glasses and corresponding corrosion rims. It is located at 22.8 eV in both corroded and pristine Ab15 Glass, which is close to the position in the dry albite glass at 23.8 eV. Contrary, in the TG pristine glass and corrosion rim the position of feature *c* is at 25.8 eV, which is in

accordance with its location in the albite glass with 5 wt% H_2O (25·6 eV). All NEXAFS features and their positions are compiled in Table 6.

4.6 *Ab initio* modelling of the O K- edge. We simulated a series of O K- edge NEXAFS spectra for simple model molecules $Si_2O_{7-x}(OH)_x$ (Fig. 14a) and $Si_2O_{7-x}(ONa)_x$ (Fig. 14b) with x ranging between 1 and 6 in order to interpret the measured O k-edge NEXAFS. The orthogonal coordinates of the model molecules are given in Table 5a, b.

The main-edge maxima of both model series expose a doublet with a feature *a'* at 1·2 - 1·4 eV and a feature *b'* at 2·2 - 2·6 eV. Feature *b'* is less intense in the H series compared to the Na series and at a low degree of hydration/sodination (x=1) feature *b'* is always more intense than feature *a'*. As the number of attached H and Na atoms is increased, the intensity of feature *a'* is increasing, whereas the intensity of feature *b'* stays rather constant (Fig. 15). In the case of the hydrogen series, this even leads to reversal of the relative intensities at intermediate degrees of hydration (x > 2), i.e. here, feature *a'* becomes even more intense than feature *b'*. The splitting of features *a'* and *b'* for the $Si_2O_{7-x}(OH)_x$ models is slightly larger (1·2 eV) than in the Si_2O_{7-x} $(ONa)_x$ series (1·0 eV). In the fully hydrated and sodinated molecules (x=6), only a single broad feature is visible at the main-edge maximum. For the $Si_2O_{7-x}(OH)_x$ a unique pre-edge feature *d'* is noticed at -1·2 eV, which increases in intensity the more H atoms are attached. Similarly, the $Si_2O_{7-x}(ONa)_x$ exposes a unique feature *e'* at 7·7 eV, which also increases with the number of Na atoms. All NEXAFS features and their positions are compiled in Table 5.

5. DISCUSSION

5.2 Corrosion rim thickness and transition widths

The thickness of the corrosion rim and its variation over time are needed to evaluate glass corrosion rates, whereas the shape of the transition front between corrosion rim and pristine glass helps understanding the corrosion mechanism. In the literature, a sharp textural and/or chemical transition has been taken as an argument that glass corrosion proceeds via a dissolution/re-precipitation mechanism (e.g. Hellmann et al. 2012, 2015; Geisler et al. 2010), whereas a gradual transition supports the leached layer model (Grambow, 1985). Hence, results of TEM and TXM investigations have to be compared and discussed taking into account the bias by the effective resolution (Fig. 4)

The results show, that the corrosion rim thickness of the Ab15 and TG glasses derived from TEM HAADF contrast and optical densities recorded with TXM at 536eV are similar, with the latter method yielding slightly higher values (10-30 nm; Fig. 6a; Table 2). This variability might reflect true anomalies in the corrosion rim thickness across the glass surface, which is a reasonable assumption as lamellas for TEM and TXM investigation where cut from different areas of the altered glass disk. However, rim thicknesses derived from TXM imaging at photon energies of 1080eV were determined from the same sample and a systematic shift of about 50 nm towards higher values is noticed. This is because at the high photon energies, the effective spatial resolution (60-78 nm, Table 4), is not sufficient to resolve the thin Carbon layer. Hence the inflection point for the transition rim→Pt is shifted compared to the inflection point resulting for a rim→C transition, which necessarily leads to an apparent broadening of the corrosion rim. We therefore conclude that corrosion rim thicknesses are equally precisely determined with TEM and TXM as long as the photon energies at which optical density maps are recorded are around the O K-edge threshold or lower.

Considering that a large electron/photon beam also leads to extensive artificial broadening of the contrast profiles (Fig. 4), we would expect an increase in the transition width with decreasing

spatial resolution. Indeed, this has been observed for the corrosion rim/pristine glass transitions in Ab15 and TG glasses (Fig. 6b).

Because the pri→rim transitions width in the Ab15 glass are in the same range as expected for the theoretical transition width for contrast profiles based on the effective spatial resolution (Fig. 6b), we conclude that the pri→rim transition in the Ab15 glass is (almost) as sharp as the rim→C and the C→Pt transitions, respectively.

Contrary and irrespective of the imaging method, the pri→rim transition width in the TG sample is about 50-70 nm above the value for theoretical beam induced broadening (Fig. 6b). Thus, we infer a more gradual transition in the TG sample compared to the Ab15 glass. Both the rather sharp transition in the Ab15 glass and the gradual transition in the TG sample are in agreement with the sharp and gradual concentrations profiles determined with TEM EDX for the Ab15 glass and the TG sample, respectively (Fig. 8).

5.3 Chemical changes in the corrosion rims. Whereas TEM-EDX data indicate an increase of O concentrations in the Ab15 corrosion rim (Fig. 8a), the area concentration derived from the O K-edge jumps shows a decrease in O content (Fig. 10). This discrepancy is explained with the extensive porosity noticed in the Ab15 glass corrosion rim (Fig. 1a), which leads to a decrease in O area concentration, even if the solid fraction of the corrosion rim exhibits higher O concentrations and/or density than the Ab15 pristine glass. In the case of the TG sample corrosion rim, both methods agree with the increase in O area concentration in the corrosion rim and following the TEM investigation, there is no resolvable porosity inside the corrosion rim. This implies that either particle density or O concentration is increasing in the TG corrosion rim. Therefore, chemical changes in the corrosion rim can only be evaluated qualitatively as long as particle density and porosity of the corrosion rim differ significantly from the pristine glass.

20

Another disadvantage of the TXM is the comparatively low detection limit. Na_2O concentration in the pristine Ab15 glass is already low (1·55 wt%) and hence, ΔOD values for both rim and pristine glass have high relative errors and differences in Na concentration in Ab15 corrosion rim and pristine glass are not resolved. However, for the TG sample with higher pristine Na_2O concentrations (15·19 wt%), both methods yield the same results, i.e. decreasing Na concentrations in the corrosion rim. Na depletion has often been described in surface altered layers of corroded silicate glasses (see introduction) and interestingly, we are able to detect this chemical feature by TXM. These considerations show that the efficiency of TXM as a precise chemical probe is limited by the concentration of the element of interest and the impossibility of the independent determination of porosity and particle density. However, with the help of an independent calibration, TXM has the potential of yielding absolute concentrations for an element of interest without beam-induced alteration (e.g. mass loss, crystallization) of the sample.

5.4 Molecular structural changes in the corrosion rim. If X-Ray photons are absorbed at energies close to the absorption edge, a core level electron will be excited to an unoccupied state. The energy difference between core level and excited state, i.e. the energy of the absorbed X-Ray Photon, mainly depends on the energy levels of the unoccupied states, which are influenced by the local arrangement of cations around the O atoms. Hence, O K-edge NEXAFS will record changes in the local bonding environment of O, which allows for detecting structural changes between pristine glasses and corrosion rims. We already noticed that the concentrations of network-modifying cations decreased in the corrosion rims compared to the pristine counterparts (Fig. 6, Table 3). As these are typically attached to non-bridging oxygen (NBO) we expect the network modifying cations (including hydrogen) to play a major role in the shape of the O-NEXAFS. Our *ab initio* calculation of the O K-edge of the $Si_2O_{7-x}(OH)_x$ molecules (Fig.

15a) have shown, that relative intensities of the near edge features *a'* decreases with the degree of hydration. We detected a similar decrease in intensity for the feature *a* in the O K-edge NEXAFS acquired in corrosion rim of the Ab15 glass and positions of features *a* and *a'* are in the same energy range (Table 4, 6). It has been shown that O K-edge NEXAFS results from electronic transitions from the O 1s state to O 2p antibonding states that hybridize with s, p or d orbitals of the surrounding cations (Henderson et al. 2003; Wang & Henderson 2004, and references therein). As the intensity of the higher energy feature *a* increases with increasing number of attached hydrogens, we attribute this feature to electronic transitions between the O 1s state and O 2p antibonded states hybridized with H 1s orbital (O 1s→O 2p + H 1s). This is supported by the NEXAFS spectrum of the albite glass with 5 wt% H_2O, which exposes a more intense feature *a* compared to the anhydrous albite glass (Fig. 13). However, the question arises, why in the pristine TG and Ab15 glass feature *a* is more intense than feature *b*, although water contents are likely to be very low (typically less than 0·1 wt % for silicate glasses synthesized at ambient pressures, Behrens & Stuke 2003). The results of the *ab initio* calculation of O K-edge NEXAFS show that the intensity increase of feature *a'* persists, if Na substitutes H in the $Si_2O_{7-x}(OH)_x$ molecules. (Fig. 15b). We therefore conclude that the electronic transition from the O 1s state to the O 2p antibonded state that hybridizes with the Na 3s orbital (O 1s→O 2p + Na 3s) provides an electronic transition in the same energy range as the O 1s→O 2p + H 1s transition. Therefore, exchanging Na with H would leave the feature *a'* intensity rather unaffected as long as the number of Si-ONa and/or Si-OH and hence, the number of non-bridging oxygens (NBO) remains unchanged. Therefore, a reasonable explanation for the Ab15 glass NEXAFS is the decrease of NBO in the corrosion rim, which is likely due to the decay of Silanol (Si-OH) bonds, which polymerize to Siloxane bonds (Si-O-Si) as postulated by Grambow et al. (1985) via

(5)   2 Si-OH → Si-O-Si + H_2O or 2 Si-O-Na → Si-O-Si + Na_2O(aq)

Such a re-condensation process might also introduce the formation of pores in the Ab15 corrosion rim (Fig. 3a). As we detected a significant increase of relative O concentration in the Ab15 corrosion rim (Fig. 8a), incorporation of additional O prior to re-condensation is likely. The same increase in O has been observed in the TG sample corrosion rim (Fig. 8b, Fig. 10), but here the intensity ratio of feature *a* and *b* in the O K- edge NEXAFS exhibits no significant changes compared to the pristine glass (Fig. 13). At the same time, we detected a significant loss of Na in the corrosion rim with both TXM and TEM. This loss is likely achieved by H/Na counter-diffusion leaving the number of NBO and hence, relative intensities of features *a* and *b* unchanged. This counter-diffusion would also explain increased O concentrations in the TG sample corrosion rim (Fig. 8b, Fig. 10), as diffusion of water into the pristine glass is required. We speculate that once the TG sample reaches a critical hydrated state, it eventually starts re-polymerizing as observed in the Ab15 glass. Hence, we interpret the corrosion rim of the TG sample as a less "mature" variety of the Ab15 glass corrosion rim with major structural re-polymerization being still absent.

However, we do not preclude a dissolution-re-precipitation mechanism for the formation of the Ab15 corrosion rim. In that case, structural differences (less bridging oxygens) and textural changes (porosity) would simply result from precipitation out of the solution. Such a mechanism is much faster compared to alteration initiated by solid-state diffusion and would also explain why the corrosion rim of Ab15 glass is growing so fast (350 nm in 1 hour).

Irrespective of the porosity-creating process, diffusion of cations is dramatically enhanced once porosity has evolved. If diffusion is faster than the progression of the alteration front, the distribution of cations across the corrosion rim/pristine glass interface is expected to be sharp on a nanometer scale. This situation is realized in the Ab15 glass altered for 1 hour, where sharp concentration profiles (Fig. 6, Fig. 8a) coincide with the sharp textural boundary between

corrosion rim and pristine glass (Fig. 1a). Contrary, cation transport during alteration of the TG sample is much slower as porosity has not (yet) evolved and solid-state diffusion is less effective than diffusion through pore space. In combination with a slowly growing corrosion rim (~130 nm in 192 hours), sigmoidal concentration profiles would tend to be preserved. This is in line with the sigmoidal Na/O concentration profile recorded with the TEM (Fig. 8b) and the higher transition width detected in TEM and TXM contrast profiles (Fig. 6b).

6. CONCLUSIONS AND OUTLOOK

TXM can be used to study the chemistry of glass samples and corrosion rims, which are not stable during standard TEM-EDX investigations, at almost the same spatial resolution as in standard transmission electron microscope. TXM has proven to be a valuable tool for the determination of corrosion rim thicknesses and qualitative chemical changes between corrosion rim and pristine glasses. With TXM, NEXAFS spectroscopy of corrosion rims is possible and thus, also structural changes on the atomic scale can be studied.

Further optimization of parameters, such as exposure time and the thickness of the FIB lamellas could improve the signal/noise ratio of the measurements in the TXM. The new TXM beamline at HZB Berlin (start of user operation planned for 2017) uses an improved monochromator and attains a higher photon flux particularly for energies > 600 eV. In combination with a proper calibration using suitable reference materials, quantitative chemical information based on edge-jump height are then derived more efficiently. Due to a better signal/noise ratio, other absorption edges such as Ca-L and Mg-K edges would become accessible for NEXAFS spectroscopy of corroded glasses as well, even at low element concentrations.

Contrast profiles recorded in this study with both TEM and TXM indicate a substantial bias by beam size effects and might also suffer from off-perpendicular orientations between glass lamella and beam during TXM investigations. In combination with X-Ray tomography, however, it could be assured that profiles are measured perfectly perpendicular to the interface. This would additionally improve the effective spatial resolution, which is needed to determine the exact shape of the pristine glass/corrosion rim interface.

7. ACKNOWLEDEGMENT

8. REFERENCES

Behrens, H., & Stuke, A. Quantification of H_2O contents in silicate glasses using IR spectroscopy – a calibration based on hydrous glasses analyzed with Karl-Fischer Titration. *Glass Sci. Technol.*, 2003, **76**, 176-189.

Bourcier, W.L., Pfeiffer, D.W., Knauss, K.G., McKeegan, K.D. & Smith, D.K. A kinetic model for borosilicate glass dissolution affinity of a surface alteration layer. *Scientific Basis for*

Nuclear Waste Management XIII, Eds V.M. Oversby & P.W. Brown, Material Research Society Symposia Proceedings,1990, **176**, 209-216.

Burnau, O. & Joly, Y. Self-consistent aspects of x-ray absorption calculations. *J. Phys.- Condens. Mat.*, 1990, **21**, 345501.

Cailleteau, C., Angeli, F., Devreux, F., Gin, S., Jestin, J., Jollivet, P. & Spalla, O. Insights into silicate-glass corrosion mechansims. *Nat. Mater.*, 2008, **7**, 978-983.

Cheng, S., Yang, G., Zhao, Y., Peng, M.Y., Skibsted, J. & Yue, Y. Quantification of the boron speciation in alkali borosilicate glasses by electron energy loss spectroscopy. *Sci. rep.*, 2015, **5**, 17526.

Dahlgren, R.A., Saigusa, M. & Ugolini, F.C. The nature, properties and management of soils, *Adv. Agron.*, 2004, **82**, 113-182.

DeNatale, J.F. & Howitt, D.G. A mechanism for radiation damage in silicate glasses. *Nuc. Instrum. Meth. B*, 1984, **1**(2-3), 489-497.

Fisher, R.V. & Schmincke, H.-U. *Pyroclastic Rocks, Springer,* 1984, 472 pp.

Fluegel, A. (2008) Global Model for Calculating Room-Temperature Glass Density from the composition. *J. Am. Ceram. Soc.*, 2008, **90**, 2622-2625.

Frugier, P., Gin, S., Minet, Y., Chave, T., Bonin, B., Godon, N., Lartigue, J.-E., Jollivet, P., Ayral, A., De Windt, L. & Santarini, G. (2008) SON68 nuclear glass dissolution kinetics: Current state of knowledge and basis of the new GRAAL model. *J. Nucl. Mater.*, 2008, **380**, 8-21.

Garvie, L. A. J. Can electron energy-loss spectroscopy (EELS) be used to quantify hydrogen in minerals from the O *K* edge? *Am. Mineral.*, 2010, **95**, 92-97.

Geisler, T., Janssen, A., Schreiter, D., Stephan, T., Berndt, J. & Putnis, A. Aqueous corrosion of borosilicate glass under acidic conditions: A new corrosion mechanism. *J. Non-Cryst. Solids*, 2010, **356**, 1458-1465.

Gin, S., Ryan, J.V., Schreiber, D.K., Neeway, J. & Cabié, M. Contribution of atom-probe tomography to a better understanding of glass alteration mechanisms: Application to a nuclear glass specimen altered 25 years in a granitic environment. Chem. Geol., 2013, **349-350**, 99-109

Grambow, B. A general rate equation or nuclear waste glass corrosion. *Scientific basis for nuclear waste management VIII*, Eds C.M. Jantzen, J.A. Stone & R.C. Ewing, Material Research Society Symposia Proceedings, 1985, **44**, 16-27.

Grambow, B. & Müller, R. (2001) First-order dissolution rate law and the role of surface layers in glass performance assessment. *J. Nucl. Mater.*, 2001, **298**, 112-124.

Guttmann, P., Bittencourt, C., Rehbein, S., Umek, P., Ke, X., van Tendeloo, G., Ewels, C.P. & Schneider, G. Nanoscale spectroscopy with polarized X-rays by NEXAFS-TXM. *Nat. Photonics*, 2012, **6**, 25-29.

Hellmann, R., Wirth, R., Daval, D., Barnes, J-P., Penisson, J.-M., Tisserand, D., Epicier, T., Florin, B. & Hervig, R.L. Unifying natural and laboratory chemical weathering with interfacial dissolution reprecipitation: A study based on the nanometer-scale chemistry of fluid silicate interfaces. *Chem. Geol.*, 2012, **294-295**, 203-216.

Hellman, R., Cotte, S., Cadel, E., Malladi, E., Karlsson, L.S., Lozano-Perez, S., Cabié, M. & Seyeux, A. Nanometre-scale evidence for interfacial dissolution-reprecipitation control of silicate glass corrosion. *Nat. Mater.*, 2015, **14**, 307-311.

Henderson, G.S., Liu, X., Fleet, M.E. Titanium coordination in silicate glasses investigated using O K-edge X-Ray absorption spectroscopy. *Mineral. Mag.*, 2003, **67**, 597-607.

Hitchcock, A.P. (1997) aXis 2000 available at http://unicorn.mcmaster.ca/aXis2000.html

Jégou, C., Gin, S. & Larche, F. Alteration kinetics of a simplified nuclear glass in an aqueous medium: effects of solution chemistry and of protective gel properties on diminishing the alteration rate. *J. Nucl. Mater.*, 2000, **280**, 216-229.

Jiang, N., Qiu, J., Ellison, A. & Silcox, J. Fundamentals of high-energy electron-irradiation-induced modifications of silicate glasses. *Phys. Rev. B*, 2003, **68**(6), 064207.

LeGuillou, C., Dohmen, R., Rogalla, D., Müller, T., Vollmer, C. & Becker, H.-W. New experimental approach to study aqueous alteration of amorphous silicates at low reaction rates. *Chem. Geol.*, 2015, **412**, 179-192.

Majorovitz, E., Angert, I., Kaiser, U. & Schröder, R.R. Benefits and limitations of low-kV macromolecular imaging of frozen-hydrated biological samples. *Biophys. J.*, 2016, **110**(4), 776-784.

Manara, A., Antonini, M., Camagni, P. & Gibson, P.N. Radiation damage in silica-based glasses: Point defects, microstructural changes and possible implications on etching and leaching. *Nuc. Instrum. Meth. B*, 1984, **1**(2-3), 475-480.

Munier, I., Croivoisier, J.-L., Grambow, B., Fritz, B. & Clément, A. Modelling the alteration Gel composition of simplified borosilicate glasses by precipitation of an ideal solid solution in equilibrium with the leachant. *J. Nucl. Mater.*, 2004, **324**, 97-115.

Orlova, G.P. Solubility of water in albite melts under pressure. *Int. Geol. Rev.*, 1964, **6**, 254-258.

Parruzot, B., Jollivet, P., Rébiscoul, D. & Gin, S. Long-term alteration of basaltic glass: Mechanism and rates. Geochim. Cosmochim. Ac., 2015, **154**, 28-48.

Rébiscoul, D., Van der Lee, A., Rieutord, F., Né, F., Spalla, O., El-Mansouri, A., Frugier, P., Syral, A. & Gin, S. Morphological evolution of alteration layers formed during nuclear

glass alteration: new evidence of a Gel as a diffusive barrier. *J. Nucl. Mater.*, 2004, **326**, 9-18.

Stöger-Pollach, M. Low voltage TEM: Influences on electron energy loss spectrometry experiments. *Micron*, **41**(6), 2010, 577-584.

Sun, K., Wang, L.M., Ewing, R.C. & Weber, W.J. Electron irradiation induced phase separation in a sodium borosilicate glass. *Nuc. Instrum. Meth. B*, 2004, **218**, 368-374.

Valle, N., Verney-Carron, A., Sterpenich, J., Libourel, G., Deloule, E. & Jollivet, P. Elemental and isotopic (^{29}Si and ^{18}O) tracing of glass alteration mechanisms. Geochim. Cosmochim. Ac., 2010, **74**, 3412-3431.

Wang, H. & Henderson, G.S. Investigation of coordination number in silicate and germinate glasses using O K-edge X-ray absorption spectroscopy. *Chem. Geol.*, 2004, **213**, 17-30.

Werme, L., Björner, I.K., Bart, G., Zwicky, H.U., Grambow, B., Lutze, W., Ewing, R.C. & Magrabi, C. Chemical Corrosion of highly radioactive borosilicate nuclear waste glass under simulated repository conditions. *J. Mater. Res.*, 1990, **5**, 1130-1146.

Wiederhorn, S.M., & Townsend, P.R. Crack healing in glass. *J. Am. Ceram. Soc.*, 1970, **53**, 486-489.

Table 1. Compositions of the pristine glasses used for the corrosion experiments determined by electron microprobe analysis (EMPA).

Oxide wt%	Ab90 n = 70	Ab15 n = 80	Technical Glass n = 50
SiO_2	66·86(33)	39·34 (25)	72·11 (56)
Al_2O_3	19·9(1)	38·16 (22)	1·02 (2)
Na_2O	9·78(10)	1·55 (4)	15·19 (14)
K_2O	n.d.	n.d.	0·33 (2)
CaO	2·03(2)	14·84 (4)	5·71 (6)
MgO	1·33 (3)	5·49 (5)	4·69 (7)
Total	99·91(40)	99·37 (44)	99·06 (55)
Cation proportions	$Na_{0·84}Ca_{0·10}Mg_{0·09}$ $Al_{1·04}Si_{2·92}O_8$	$Na_{0·14}Ca_{0·74}Mg_{0·38}$ $Al_{2·10}Si_{1·83}O_8$	$Na_{1·35}K_{0·02}Ca_{0·28}Mg_{0·32}$ $Al_{0·06}Si_{3·31}O_8$

Standard deviation (1 SD) of n measurements in brackets. Cation proportions obtained by normalization to 8 O.

Table 2. Thickness of corrosion rims and width of the transition to the pristine glass determined with transmission electron microscopy (TEM) and transmission X-Ray microscopy (TXM).

Imaging method	Ab15 (1 h)						TG (192 h)					
	pixel size	eff. res.[a]	transition width[b] rim→C	(rim)/C→Pt	rim→pri	rim thickn.	pixel size	eff. res.[a]	transition width[b] rim→C	(rim)/C→Pt	rim→pri	rim thickn.
TEM HAADF	2	24	34	26	58	316	2	24	30	50	106	126
TXM OD$_{536\,eV}$	12·5	44	40	68	78	345	12·5	44	54	94	116	136
TXM OD$_{1080\,eV}$	29	78	carbon not res.	(112)	104	397	23	60	carbon not res.	(86)	140	175

Note: All values in nm
[a] effective spatial resolution (see discussion)
[b] Values in brackets in column (rim)/C→Pt were determined for the rim→Pt transition as the Carbon layer is not resolved. The other values represent C→Pt transition widths.
Rim thickness and transition width are determined on the basis of a sigmoidal fit of the averaged contrast profiles (Fig. 2). For more information see text.

Table 3. Densities of pristine glasses and thickness of lamellas analyzed with TEM and TXM. Edge jumps across Na and O K-edges as determined with TXM and area concentrations of Na and O.

Glass	density (g/cm^3)	lamella thickness (nm)		edge jump ($\Delta\mu d$)				concentration (atoms/cm$^2 \times 10^{18}$)			
		Na K-edge	O K-edge	Na K-edge		O K-edge		Na		O	
				pristine	*rim*	*pristine*	*rim*	*pristine*	*rim*	*pristine*	*rim*
Ab15	2·67[a]	~ 1000	~ 200	0·04 (2)	0·02 (1)	0·67 (1)	0·48 (1)	0·08	0·06 (1)[c]	1·23	0·93 (9)[c]
Ab90	2·42	~ 1000	~ 200	0·13 (3)	no rim	0·58 (2)	no rim	0·41	no rim	1·12	no rim
TG	2·47	~ 1000	~ 200	0·21 (3)	0·12 (2)	0·63 (1)	0·76 (1)	0·66	0·38 (6)[c]	1·11	1·47 (15)[c]
Ab100	2·39	n.a.	~ 500	n.a.		1·30 (2)	no rim	n.a.	no rim	2·77	no rim
Ab100 + 5wt% H$_2$O	2·33[b]	n.a.	~ 500	n.a.		1·52 (2)	no rim	n.a.	no rim	2·82	no rim

Densities calculated from Fluegel, 2008 using the average compositions given in Table 1. Exceptions are:
[a] Al$_2$O$_3$ content was set to 30 wt% to match the model applicabilty of Fluegel, 2008
[b] from Orlova, 1964
[c] calculated from calibration with pristine glasses (see Fig. 11)
n.a.: not analyzed

Table 4. Position of features in the O K-edge NEXAFS spectra of glasses obtained with TXM.

Glass	Feature		
	a	b	c
Ab15			
pristine	1·4	4·8	22·8
rim	2·2	4·8	22·8
Technical Glass			
pristine	2·2	5·2	25·8
rim	2·2	4·8	25·8
Albite glass			
+ 5 wt% H$_2$O	1·8	4·8	25·6
+ 0 wt% H$_2$O	1·8	4·8	23·8

Note: Energies are given in ΔeV relative to the threshold energy of the O K-edge NEXAFS for Quartz at 537 eV. Positions refer to the NEXAFS spectra presented in Fig. 13.

Table 5a. Orthogonal coordinates of the $Si_2O_{7-x}(OH)_x$ molecule used for the *ab initio* O K- edge NEXAFS calculation (Fig. 14a)

Atom	Orthogonal coordinates [Å]		
	x	y	z
H1	-0·063	-9·149	0·692
H2	-0·204	-6·458	-1·246
H3	1·846	-9·803	-1·482
H5	2·722	-3·284	1·487
H6	0·777	-4·391	-0·966
H7	4·663	-3·872	-0·678
O1	0·576	-8·439	0·871
O2	0·382	-7·179	-1·532
O3	2·326	-9·037	-1·124
O4	2·464	-6·625	0·13
O5	2·568	-4·244	1·44
O6	1·73	-4·337	-1·147
O7	4·347	-4·781	-0·547
Si1	1·436	-7·82	-0·413
Si2	2·778	-4·997	-0·031

Table 5b. Orthogonal coordinates of the $Si_2O_{7-x}(ONa)_x$ molecule used for the *ab initio* O K- edge NEXAFS calculation (Fig. 14b)

Atom	orthogonal coordinates [Å]		
	x	y	z
Na1	-2·242	5·931	-1·834
Na2	-3·855	6·562	2·528
Na3	-2·337	2·604	1·094
Na5	-11·258	6·260	-1·765
Na6	-9·842	6·669	2·400
Na7	-11·282	2·877	1·279
O1	-4·430	4·953	-1·673
O2	-5·186	5·381	0·904
O3	-4·503	2·884	0·093
O4	-6·821	4·011	-0·778
O5	-9·174	5·077	-1·634
O6	-8·355	5·473	0·930
O7	-9·181	3·006	0·132
Si1	-8·383	4·391	-0·337
Si2	-5·234	4·310	-0·364

Table 6. Position of features in the calculated O K-edge NEXAFS of model compounds

Model molecules	Feature			
	a'	b'	d'	e'
$Si_2O_{7-x}(OH)_x$	1·4	2·6	-1·2	/
$Si_2O_{7-x}(ONa)_x$	1·2	2·2	/	7·7

Note: Energies are given in ΔeV relative to the threshold energy of the O K-edge NEXAFS for Quartz at 537 eV. Positions refer to the NEXAFS spectra presented in Fig. 15.

Ab15

Technical glass
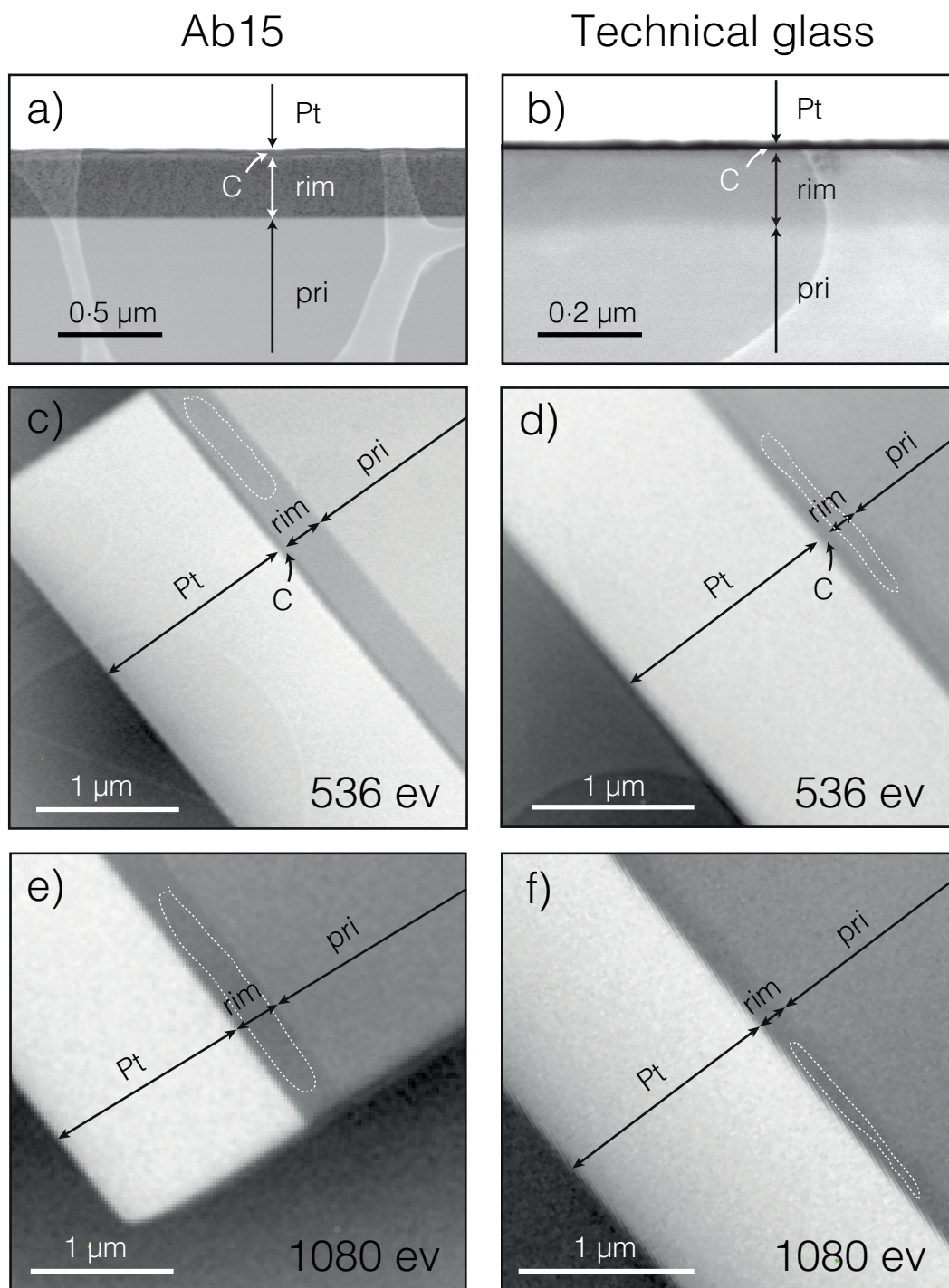
Figure 1. Corroded Ab15 and TG glasses imaged with TEM in HAADF mode (a,b) and optical densities recorded with TXM at photon energies of 536 eV (c,d) and 1080 eV (e,f). The layers are denoted as follows: pristine glass (pri), corrosion rim (rim), carbon (C), and platinum (Pt). Region of interest for O and Na K-edge NEXAFS spectra of corrosion rims are marked by dotted lines.
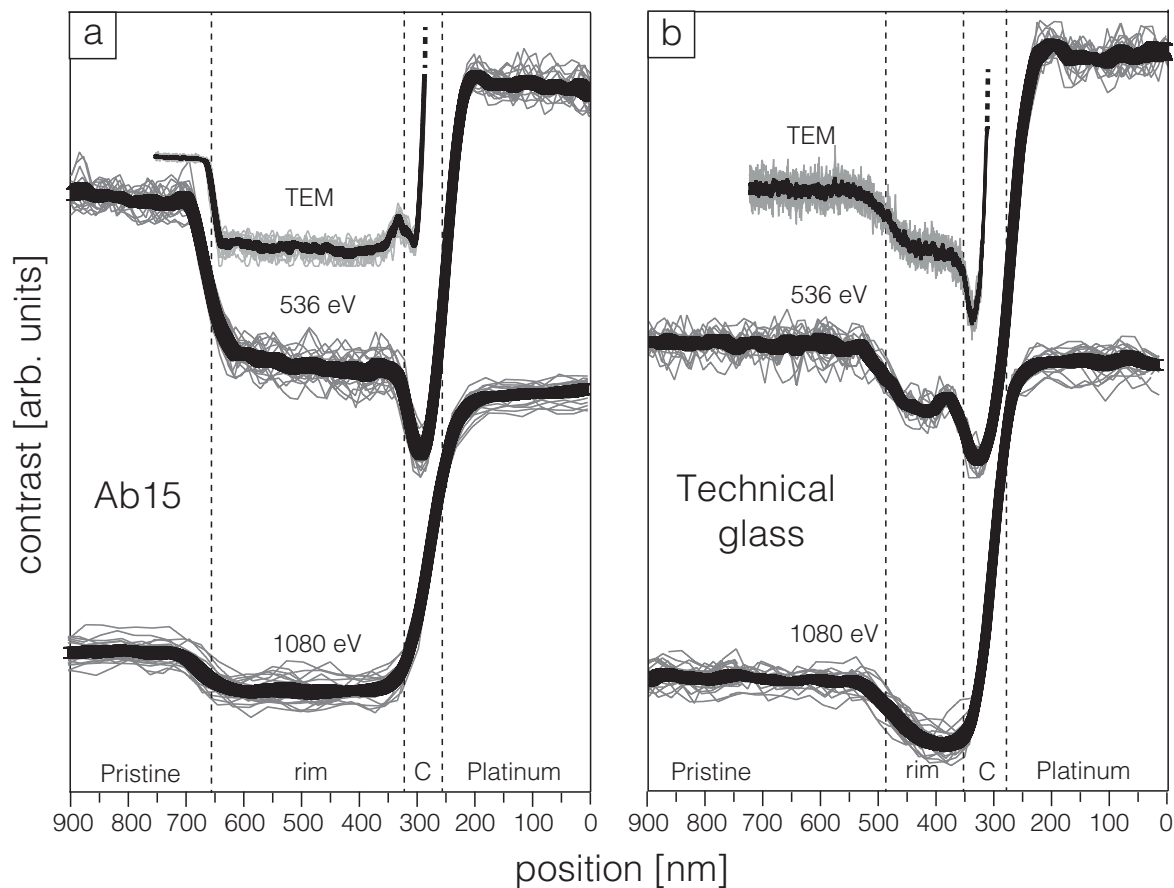
Figure 2. TEM HAADF contrast and optical density profiles perpendicular to the alteration front. Optical density profiles were recorded at photon energies of 536 eV (O K-edge) and 1080 eV (Na K-edge). For each profile, 20 individual profiles (grey) were averaged resulting in the black line, which includes 95% confidence interval. Approximate layer boundaries are indicated with dotted lines. For the sake of clarity profiles are offset vertically and the high contrast region of the TEM HAADF profiles was cut.
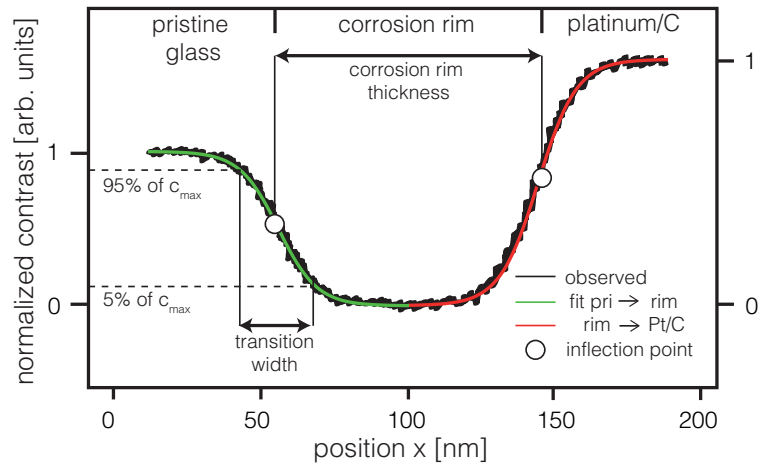
Figure 3. Schematic illustration of the data processing for the contrast profiles presented in Figure 2. Each profile was normalized to a contrast jump of 1 and a sigmoidal function was fitted to each transition to derive corrosion rim thickness and transition width.
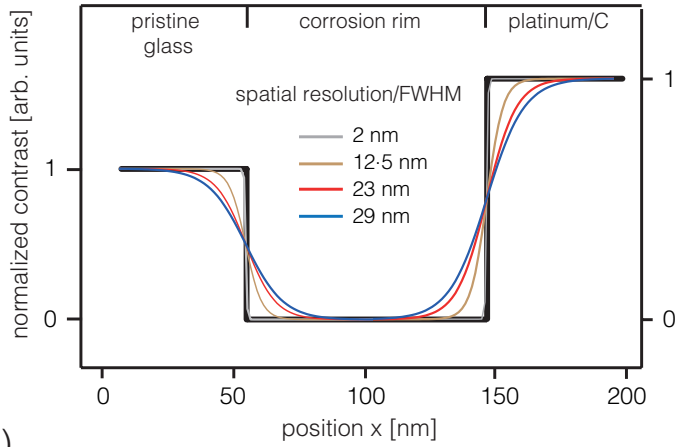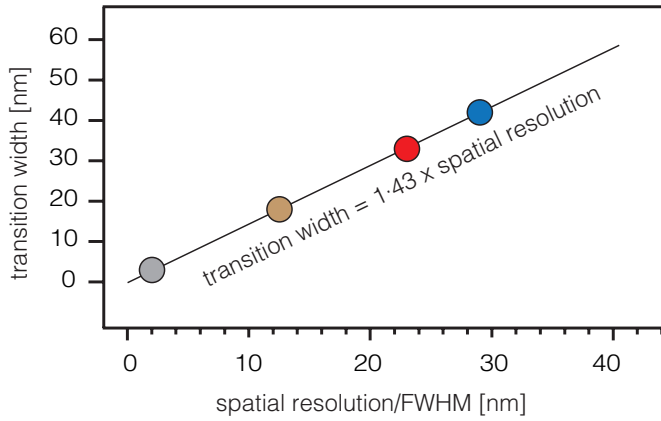
Figure 4. a) Apparent increase of the transition width with spatial resolution for a perfectly sharp contrast step (black line) if imaged with a Gaussian shaped beam. The full width at half maximum (FWHM) corresponds to the image pixel size of the imaging methods presented in this study (see Table 4). b) Linear correlation of the transition width with spatial resolution, i.e. FWHM of the Gaussian-shaped beam. The colours correspond to the contrast profiles in a).
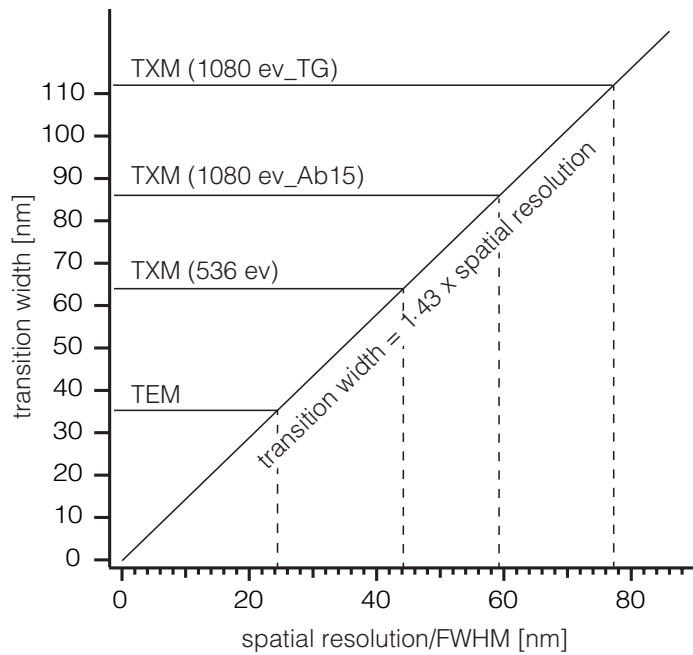
Figure 5. Effective spatial resolution (dashed lines) of the different imaging methods obtained from the average transitions widths determined for the sharp transitions from the corrosions rims to the carbon layer and from the carbon layer to the platinum layer (solid lines, see Table 2).
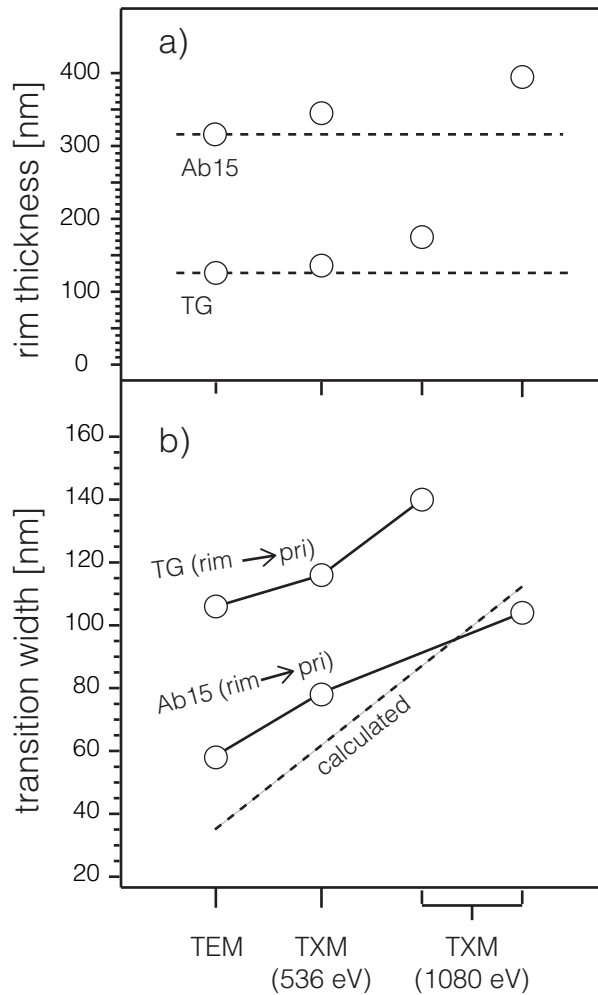
Figure 6. a) Thickness of the corrosion rim of the Ab15 glass altered for 1 hour and of the TG sample altered for 192 hours, determined from the contrast profiles recorded with TEM and TXM. Vertical dashed lines are a guide to the eye. b) Width of the contrast transition from corrosion rim to pristine glasses. The dashed line indicates the theoretical broadening of a perfectly step like profile based on the effective spatial resolution (see discussion). Image pixel size varied between TXM analyses of Ab15 and TG samples at 1080 eV (see Table 2). Accordingly, the ordinate comprises two separate points.
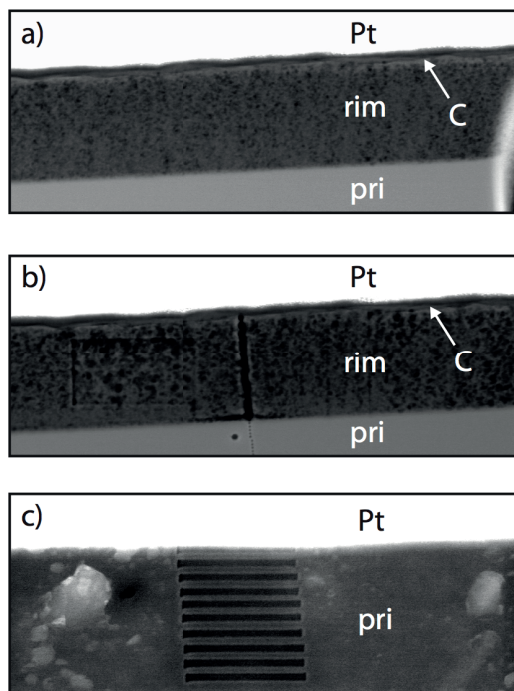
Figure 7. Irradiation damage during TEM investigation. a) Ab15 glass altered for 1 hour before and b) after EDX analyses (line and box scan). c) crystallization induced by the electron beam during investigation of the Ab90 glass.
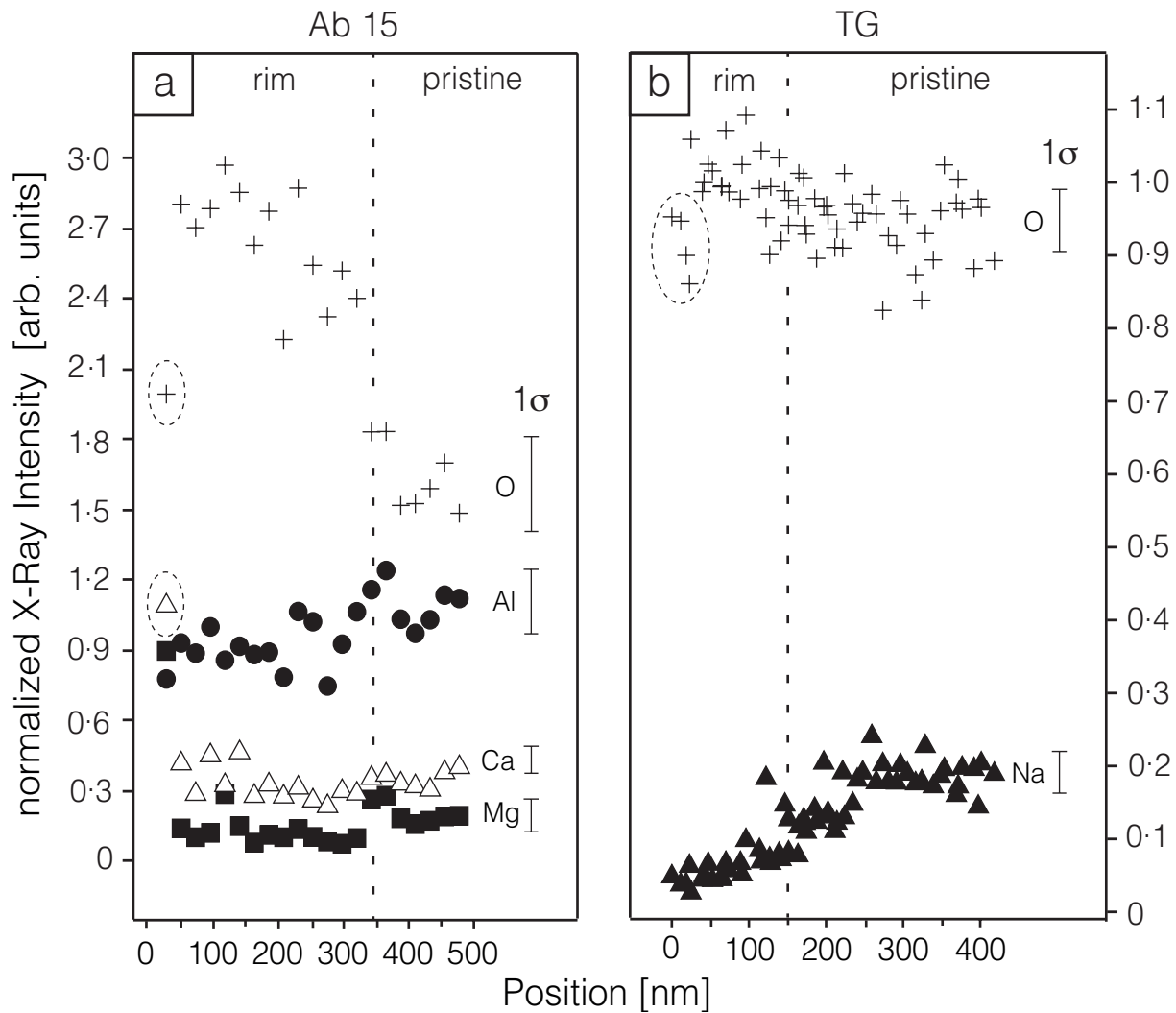
Figure 8. TEM EDX profiles recorded across the transition from pristine glass to corrosion rim and normalized to the Si K_α – intensity. For the TG sample three individual profiles are presented, which were taken from different regions. Just one profile was recorded in the Ab15 glass. Encircled data points are outliers that stem from contamination by the protective platinum or carbon layer.
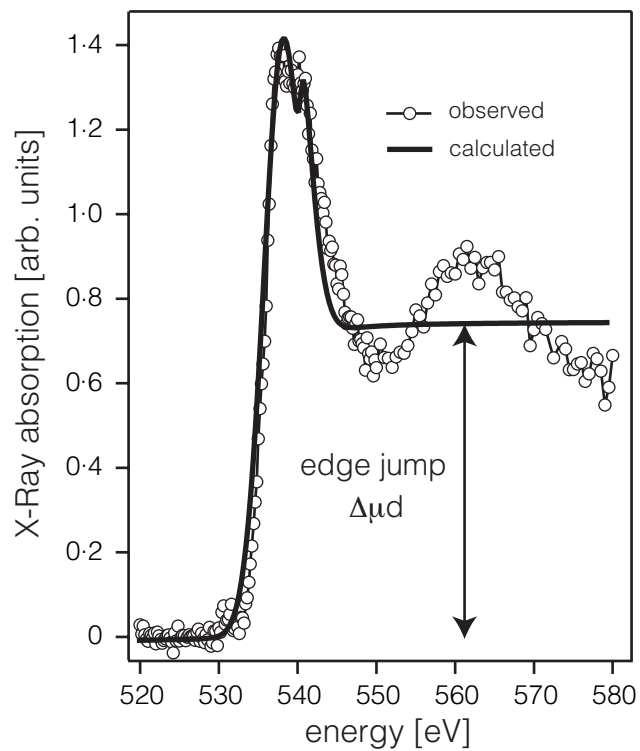
Figure 9. O K-edge NEXAFS spectrum of the corrosion rim of the TG sample (open circles) corrected with a linear pre-edge background. Combination of an *arctan* function and two pseudovoigt functions resulted in the fitted spectra (solid line). The height of the edge jump ($\Delta\mu d$) is proportional to the volume concentration of O.
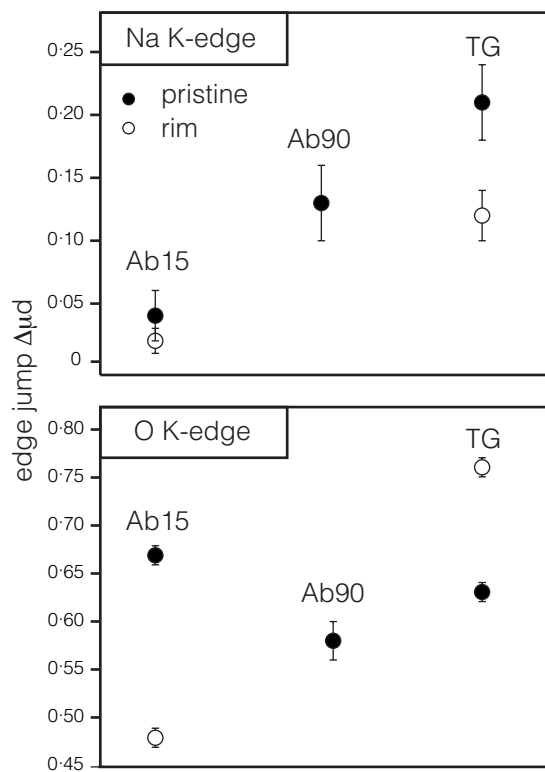
Figure 10. Edge jumps (Δμd) from fitting of the NEXAFS spectra at Na and O K-edges. Spectra were collected from regions of interest indicated in Figure 1.
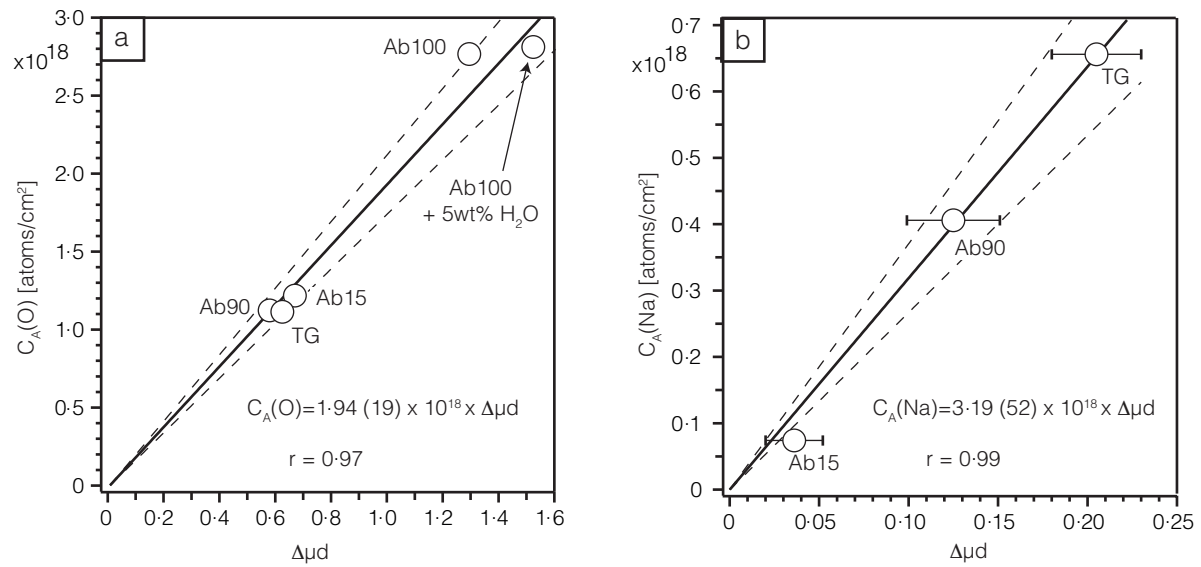
Figure 11. Edge jumps of the pristine glasses vs. concentration of O and Na. A linear fit (straight line) was applied as a calibration to obtain unknown concentrations in the Ab15 and TG sample corrosion rim (see Table 3). The lines were forced through the origin. Confidence bands (95%) are shown as dotted lines. The regression equations (including 95% confidence interval) are indicated in the figure.
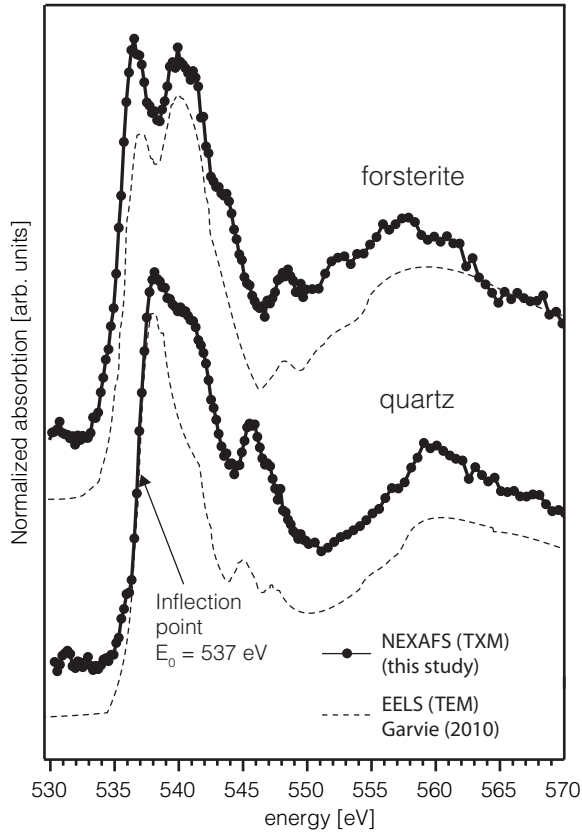
Figure 12. Normalized O K- edge NEXAFS of quartz and forsterite recorded with TXM compared to O K- edge EELS spectra recorded with TEM (Garvie, 2010). The inflection point of the edge jump of the quartz NEXAFS at 537 eV is used for calibration of all O K- edge NEXAFS presented in this study.
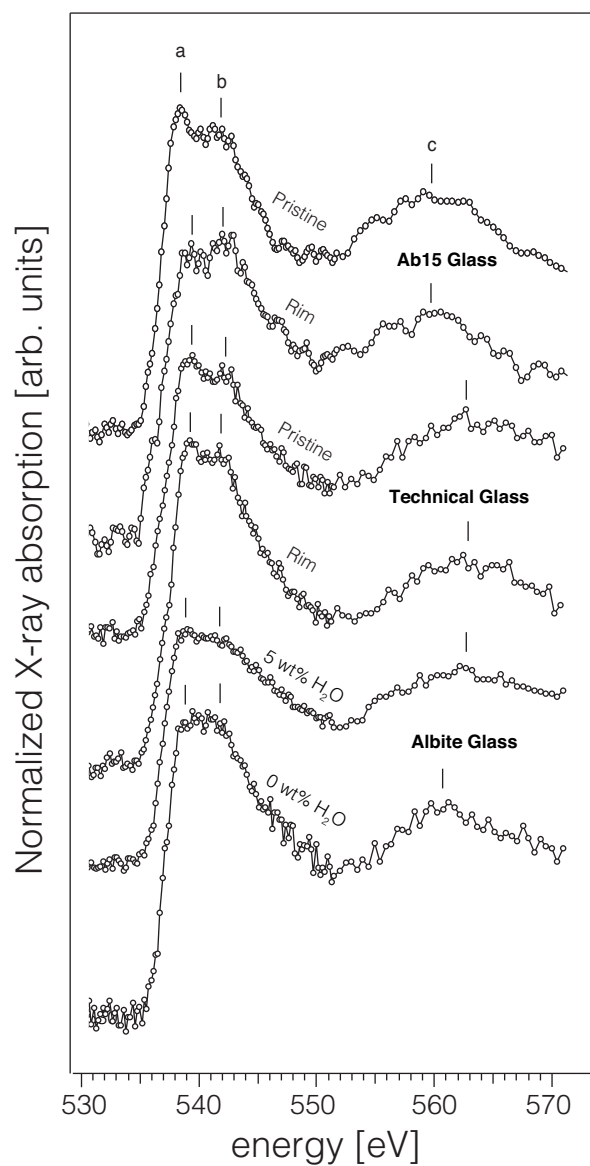
Figure 13. Normalized O K-edge NEXAFS of the pristine Ab15 and TG samples and their corrosion rims recorded with TXM. Reference spectra of dry albite glass and albite glass with 5 wt% H_2O were also obtained for comparison. For further explanation see text.

a)

b)

<Si-O> = 1·67 Å
<O-H> = 0·97 Å

<Si-O> = 1·67 Å
<O-Na> = 2·40 Å
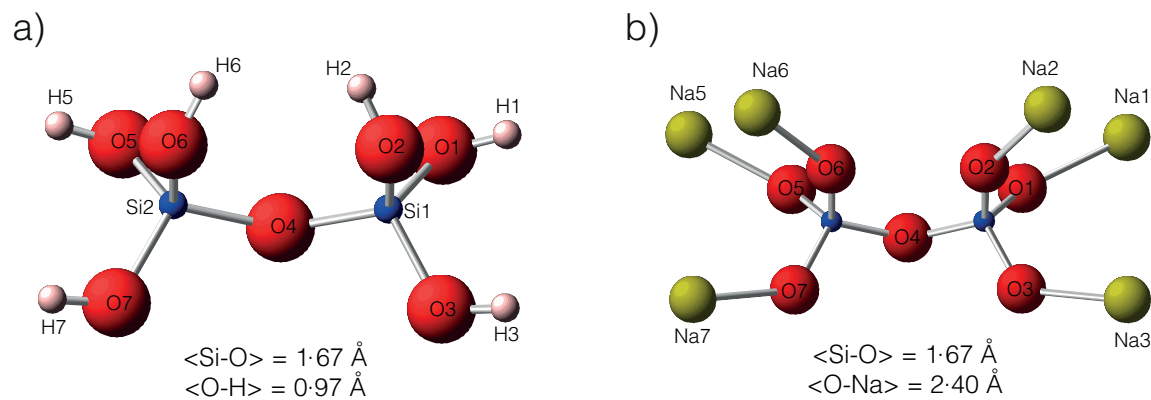
Figure 14. $Si_2O_{7-x}(OH)_x$ and $Si_2O_{7-x}(ONa)_x$ molecules used for the *ab initio* calculation of the O K- edge NEXAFS with the FDMNES computer code. "x" indicates the number of attached H/Na atoms (here, all 6 H/Na atoms are attached). Si-O and O-H/O-Na distances are indicated in the figure. Corresponding orthogonal coordinates are given in Table 5a,b.
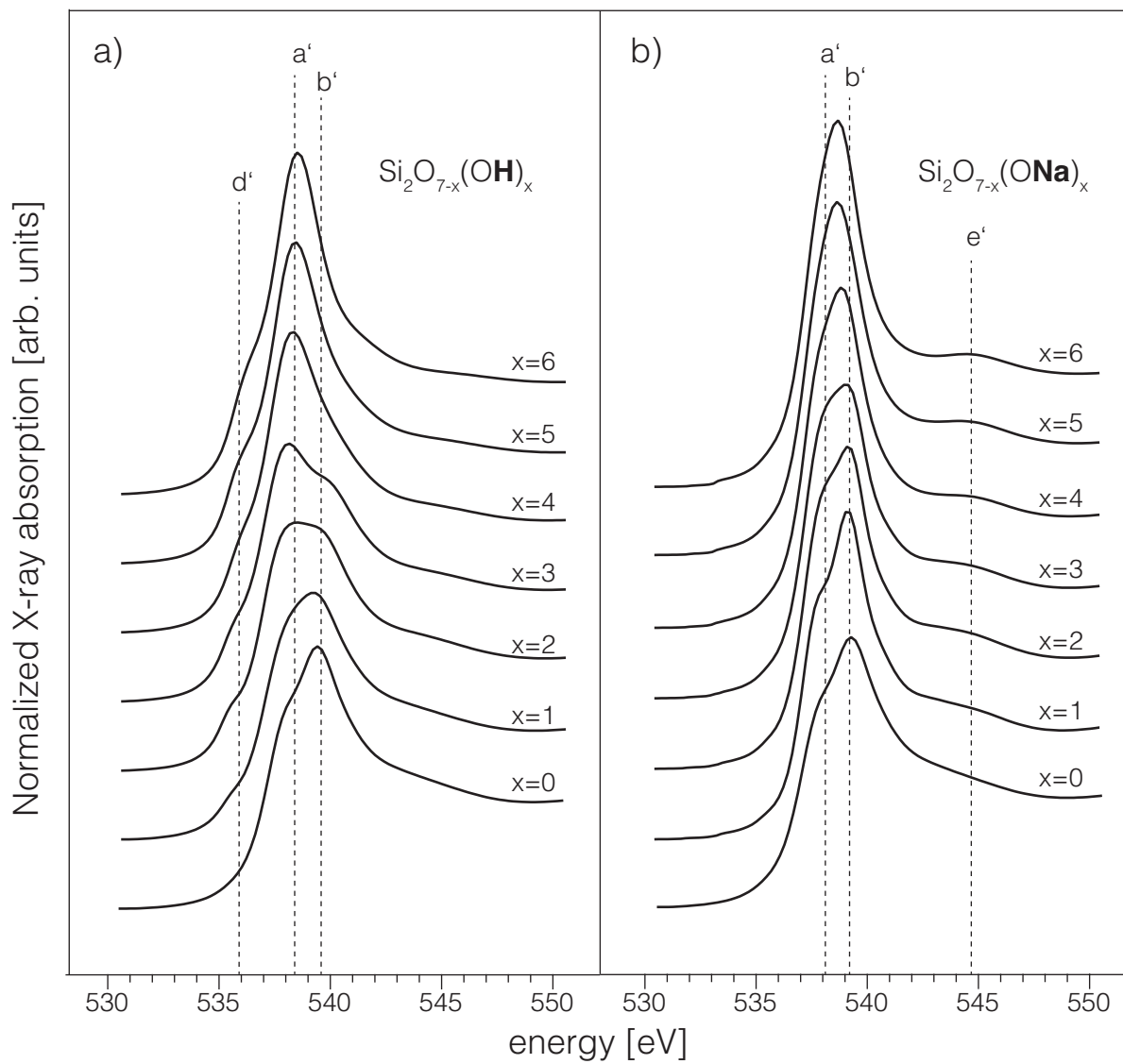
Figure 15. Calculated O K-edge NEXAFS of the $Si_2O_{7-x}(ONa)_x$ (a) and $Si_2O_{7-x}(OH)_x$ (b) model molecules. For further explanation see text.